THE JOURNAL OF BIOLOGICAL CHEMISTRY VOL. 284, NO. 4, pp. 2472–2481, January 23, 2009

Structural Insights into Ca^{2+}-dependent Regulation of Inositol 1,4,5-Trisphosphate Receptors by CaBP1*

Received for publication, August 22, 2008, and in revised form, November 4, 2008 Published, JBC Papers in Press, November 13, 2008, DOI 10.1074/jbc.M806513200

Congmin Li[‡], Jenny Chan[§], Franciose Haeseleer[¶], Katsuhiko Mikoshiba[‖], Krzysztof Palczewski[**], Mitsuhiko Ikura[§], and James B. Ames[‡1]

*From the [‡]Department of Chemistry, University of California, Davis, California 95616, the [§]Division of Signaling Biology, Ontario Cancer Institute and Department of Medical Biophysics, University of Toronto, Ontario M5G 2M9, Canada, the [¶]Department of Ophthalmology, University of Washington, Seattle, Washington 98195, the [‖]Laboratory for Developmental Neurobiology, Brain Development Research Group, Brain Science Institute, RIKEN, 351-0198 Saitama, Japan, and the **Department of Pharmacology, School of Medicine, Case Western Reserve University, Cleveland, Ohio 44106*

Calcium-binding protein 1 (CaBP1), a neuron-specific member of the calmodulin (CaM) superfamily, modulates Ca^{2+}-dependent activity of inositol 1,4,5-trisphosphate receptors ($InsP_3Rs$). Here we present NMR structures of CaBP1 in both Mg^{2+}-bound and Ca^{2+}-bound states and their structural interaction with $InsP_3Rs$. CaBP1 contains four EF-hands in two separate domains. The N-domain consists of EF1 and EF2 in a closed conformation with Mg^{2+} bound at EF1. The C-domain binds Ca^{2+} at EF3 and EF4, and exhibits a Ca^{2+}-induced closed to open transition like that of CaM. The Ca^{2+}-bound C-domain contains exposed hydrophobic residues (Leu^{132}, His^{134}, Ile^{141}, Ile^{144}, and Val^{148}) that may account for selective binding to $InsP_3Rs$. Isothermal titration calorimetry analysis reveals a Ca^{2+}-induced binding of the CaBP1 C-domain to the N-terminal region of $InsP_3R$ (residues 1–587), whereas CaM and the CaBP1 N-domain did not show appreciable binding. CaBP1 binding to $InsP_3Rs$ requires both the suppressor and ligand-binding core domains, but has no effect on $InsP_3$ binding to the receptor. We propose that CaBP1 may regulate Ca^{2+}-dependent activity of $InsP_3Rs$ by promoting structural contacts between the suppressor and core domains.

Calcium ion (Ca^{2+}) in the cell functions as an important messenger that controls neurotransmitter release, gene expression, muscle contraction, apoptosis, and disease processes (1). Receptor stimulation in neurons promotes large increases in intracellular Ca^{2+} levels controlled by Ca^{2+} release from intracellular stores through $InsP_3Rs$ (2). The neuronal type-1 receptor ($InsP_3R1$)[2] is positively and negatively regulated by cytosolic Ca^{2+} (3–6), important for the generation of repetitive Ca^{2+} transients known as Ca^{2+} spikes and waves (1). Ca^{2+}-dependent activation of $InsP_3R1$ contributes to the fast rising phase of Ca^{2+} signaling known as Ca^{2+}-induced Ca^{2+} release (7). Ca^{2+}-induced inhibition of $InsP_3R1$, triggered at higher cytosolic Ca^{2+} levels, coordinates the temporal decay of Ca^{2+} transients (6). The mechanism of Ca^{2+}-dependent regulation of $InsP_3Rs$ is complex (8, 9), and involves direct Ca^{2+} binding sites (5, 10) as well as remote sensing by extrinsic Ca^{2+}-binding proteins such as CaM (11, 12), CaBP1 (13, 14), CIB1 (15), and NCS-1 (16).

Neuronal Ca^{2+}-binding proteins (CaBP1–5 (17)) represent a new sub-branch of the CaM superfamily (18) that regulate various Ca^{2+} channel targets. Multiple splice variants and isoforms of CaBPs are localized in different neuronal cell types (19–21) and perform specialized roles in signal transduction. CaBP1, also termed caldendrin (22), has been shown to modulate the Ca^{2+}-sensitive activity of $InsP_3Rs$ (13, 14). CaBP1 also regulates P/Q-type voltage-gated Ca^{2+} channels (23), L-type channels (24), and the transient receptor potential channel, TRPC5 (25). CaBP4 regulates Ca^{2+}-dependent inhibition of L-type channels in the retina and may be genetically linked to retinal degeneration (26). Thus, the CaBP proteins are receiving increased attention as a family of Ca^{2+} sensors that control a variety of Ca^{2+} channel targets implicated in neuronal degenerative diseases.

CaBP proteins contain four EF-hands, similar in sequence to those found in CaM and troponin C (18) (Fig. 1). By analogy to CaM (27), the four EF-hands are grouped into two domains connected by a central linker that is four residues longer in CaBPs than in CaM. In contrast to CaM, the CaBPs contain non-conserved amino acids within the N-terminal region that may confer target specificity. Another distinguishing property of CaBPs is that the second EF-hand lacks critical residues required for high affinity Ca^{2+} binding (17). CaBP1 binds Ca^{2+} only at EF3 and EF4, whereas it binds Mg^{2+} at EF1 that may

* This work was supported, in whole or in part, by National Institutes of Health Grants EY012347 and NS045909 (to J. B. A.). This work was also supported by Grant RR11973 to the University of California Davis NMR Facility from the National Institutes of Health, the Canadian Institutes of Health Research and the Canada Foundation for Innovation (to M. I.), and a fellowship from the Canadian Institutes of Health Research (to J. C.). The costs of publication of this article were defrayed in part by the payment of page charges. This article must therefore be hereby marked "*advertisement*" in accordance with 18 U.S.C. Section 1734 solely to indicate this fact.

The atomic coordinates and structure factors (codes 2k7b, 2k7c, and 2k7d) have been deposited in the Protein Data Bank, Research Collaboratory for Structural Bioinformatics, Rutgers University, New Brunswick, NJ (http://www.rcsb.org/).

[1] To whom correspondence should be addressed: Dept. of Chemistry, One Shields Ave., University of California, Davis, CA 95616. Tel.: 530-752-6358; Fax: 530-752-8995; E-mail: ames@chem.ucdavis.edu.

[2] The abbreviations used are: $InsP_3R$, inositol 1,4,5-trisphosphate receptor; CaBP1, calcium-binding protein 1; HSQC, heteronuclear single quantum coherence; HMQC, heteronuclear multiple quantum coherence; $InsP_3$, inositol 1,4,5-trisphosphate; NOE, nuclear Overhauser effect; NOESY, NOE spectroscopy; GST, glutathione *S*-transferase; PDB, Protein Data Bank; ITC, isothermal titration calorimetry.

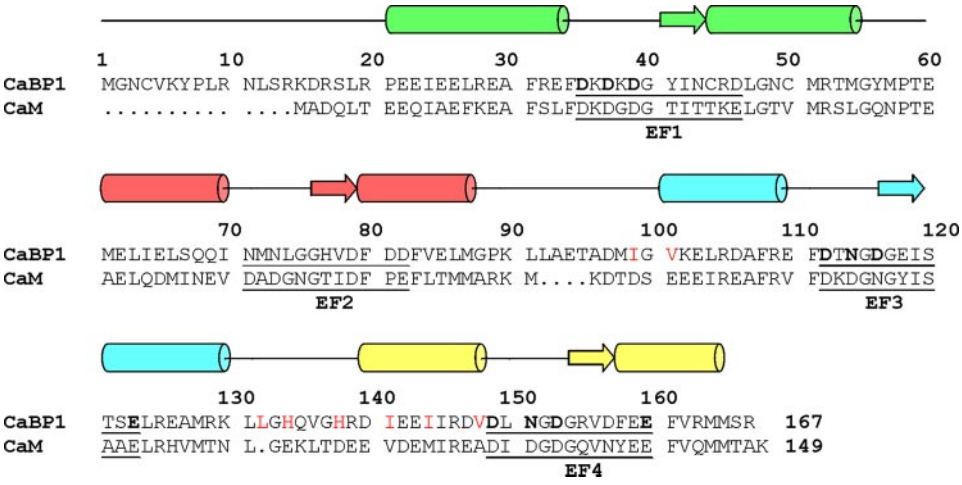

FIGURE 1. **Amino acid sequence alignment of human CaBP1 with CaM.** Secondary structural elements (α-helices and β-strands) were derived from NMR analysis. The four EF-hands (EF1, EF2, EF3, and EF4) are highlighted *green*, *red*, *cyan*, and *yellow*. Residues in the 12-residue Ca^{2+}-binding loops are *underlined* and chelating residues are highlighted *bold*. Non-conserved residues in the hydrophobic patch are colored *red*.

serve a functional role (28). Indeed, changes in cytosolic Mg^{2+} levels have been detected in cortical neurons after treatment with neurotransmitter (29). Other neuronal Ca^{2+}-binding proteins such as DREAM (30), CIB1 (31), and NCS-1 (32) also bind Mg^{2+} and exhibit Mg^{2+}-induced physiological effects. Mg^{2+} binding in each of these proteins helps stabilize their Ca^{2+}-free state to interact with signaling targets.

Despite extensive studies on CaBP1, little is known about its structure and target binding properties, and regulation of $InsP_3Rs$ by CaBP1 is somewhat controversial and not well understood. Here, we present the NMR solution structures of both Mg^{2+}-bound and Ca^{2+}-bound conformational states of CaBP1 and their structural interactions with $InsP_3R1$. These CaBP1 structures reveal important Ca^{2+}-induced structural changes that control its binding to $InsP_3R1$. Our target binding analysis demonstrates that the C-domain of CaBP1 exhibits Ca^{2+}-induced binding to the N-terminal cytosolic region of $InsP_3R1$. We propose that CaBP1 may regulate Ca^{2+}-dependent channel activity in $InsP_3Rs$ by promoting a structural interaction between the N-terminal suppressor and ligand-binding core domains that modulates Ca^{2+}-dependent channel gating (8, 33, 34).

EXPERIMENTAL PROCEDURES

Expression and Purification of CaBP1—CaBP1 has two splice variants expressed in the brain, termed l-CaBP1 and s-CaBP1 (17). Both variants regulate Ca^{2+} channels with similar efficacy (14) and the extra residues in the long variant can be deleted without affecting CaBP1 binding to $InsP_3Rs$. The short splice variant (19.4 kDa and 167 residues) is more soluble and amenable for NMR structural analysis and was used throughout this study. Recombinant CaBP1 and mutants were expressed and purified from *Escherichia coli* strain BL21(DE3) as described previously (28).

Construction of CaBP1 N-domain and C-domain Fragments—cDNAs coding for the CaBP1 N-domain (residues 1–91; CaBP1-N) and C-domain (residues 96–167; CaBP1-C) were cloned into protein expression vectors pET-28a(+) and pET-3a(+), respectively. Recombinant CaBP1-C protein was expressed and purified by the same method as full-length CaBP1. The His_6-CaBP1-N protein was purified first by nickel-Sepharose (Amersham Biosciences), and then by using Superdex 200 size exclusion chromatography.

Construction of CaBP1 Mutants—The D35A, D37A, D39A, D46A, ΔL132, H134E, and V148A mutants of CaBP1 were generated by using the QuikChange site-directed mutagenesis kit (Stratagene) and the presence of these mutations was confirmed by DNA sequencing. The mutant expression and purification procedures were the same as that for wild type.

Expression and Purification of IP_3R_{sup}-(2–223), IP_3R_{core}-(224–604), and $InsP_3R$-(1–587)—The recombinant suppressor domain ($InsP_3R_{sup}$ residues, 2–223) and ligand-binding core domain ($InsP_3R_{core}$ residues, 224–604) containing a GST tag were cloned, expressed, and purified as described by Ref. 35. The GST tag was removed by adding 1 μg of thrombin to the purified GST fusion protein sample that was then applied to a Superdex-75 size exclusion column to remove the GST tag and other impurities. A recombinant dual domain construct containing both $InsP_3R_{sup}$ and $InsP_3R_{core}$ ($InsP_3R$-(1–587)) was cloned, expressed, and purified as described (35). The recombinant $InsP_3R$-(1–587) protein contained a C-terminal intein-CBD-His_9 tag that was first purified with nickel-nitrilotriacetic acid resin (Qiagen) and the CBD-His_9 tag was cleaved by treatment with 20 mM dithiothreitol for 24 h. The cleaved protein was released from chitin beads, concentrated, and then chromatographed on a Superdex 200 column.

NMR Spectroscopy—Samples for NMR analyses were prepared by dissolving unlabeled, ^{15}N-labeled, or (^{15}N, ^{13}C)-labeled CaBP1 in 0.3 ml of 95% H_2O, 5% [^2H]H_2O containing 10 mM [$^2H_{11}$]Tris, pH 7.4, 0.1 mM KCl, and 5 mM EDTA (apo-), 5 mM $MgCl_2$ (Mg^{2+}-bound), or 5 mM $CaCl_2$, 5 mM $MgCl_2$ (Ca^{2+}-bound). All NMR experiments were performed at 30 °C on a Bruker Avance 600 MHz spectrometer equipped with triple resonance cryoprobe and z axis gradient. Backbone and side chain assignments were described previously (36, 37). All NMR data were processed and analyzed by using the programs NMRPipe and nmrView.

NMR Structure Calculation—The structures were calculated with XPLOR-NIH (38) that employed the YASAP protocol (39). Distance restraints derived from inter-proton NOEs and dihedral angles (φ and ψ) from chemical shift index data are summarized in Table 1. Distance constraints involving Ca^{2+} bound to loop residues 1, 3, 5, 7, and 12 in EF3 and EF4 (27), and Mg^{2+} bound to loop residues 1, 3, and 5 in EF1 were introduced as described previously (40). Fifty independent structures were calculated and the 15 lowest energy structures were selected. The final structural statistics are summarized in Table 1 and

coordinates were deposited into the RCSB Protein Data bank (accession numbers 2k7b, 2k7c, and 2k7d).

Isothermal Titration Calorimetry—The CaBP1 and $InsP_3R$ interactions were measured by a MicroCal VP-ITC microcalorimeter at 30 °C as described previously (28). Proteins were exchanged into buffer containing 15 mM Tris-HCl, pH 7.5, 300 mM NaCl, 3% glycerol, and 1 mM tris(2-carboxyethyl)phosphine with the addition of 2 mM EDTA (apo-state), 5 mM $MgCl_2$ (Mg^{2+}-bound state), or 5 mM $MgCl_2$ and 5 mM Ca^{2+} (Ca^{2+}-bound state). The $InsP_3R$-(1–587) at a concentration of 50–80 μM was titrated with 1–2 mM CaBP1 in 25 steps of 10 μl. The data were analyzed with a one-binding site model using MicroCal Origin 7 for ITC.

Docking Calculation—Structural modeling of the CaBP1-receptor complex (CaBP1-C·$InsP_3R_{sup}$·$InsP_3R_{core}$) was performed using ZDOCK (41). CaBP1-C (PDB 2k7d) was independently docked to either $InsP_3R$sup (PDB 1xzz) or $InsP_3R$core (PDB 1n4k). The top 20 ZDOCK predicted complexes with lowest energy were superimposed. CaBP1-C from each binary complex was structurally aligned using PyMol to generate possible ternary interactions.

RESULTS

CaBP1 Has Two Independent Domains—A critical first step in the NMR structural analysis of CaBP1 was to identify whether the four EF-hands in CaBP1 combine to form two separately folded domains: N-domain (EF1 and EF2) *versus* C-domain (EF3 and EF4) like what is seen in CaM (42). Alternatively, the four EF-hands might interact to form a single globular domain like what is observed in NCS-1 (43) and CIB1 (44). First, we analyzed the NOESY-HSQC spectra of CaBP1 and were unable to detect NOE-based contacts between the two domains, consistent with this protein having non-interacting domains.

Our second approach was to examine the backbone flexibility of the two domains and the central linker. In Fig. 2*A*, {^{1}H}-^{15}N NOE measurements indicate relatively low heteronuclear NOE values (~0.5) for residues in the central linker region (residues 92–98), suggesting that CaBP1 does indeed contain a flexible inter-domain linker. By contrast, much higher heteronuclear NOE values (~0.8) are found for residues in each domain and indicate the two domains are separately folded.

A final test for the existence of two independent domains was to analyze NMR spectra of individual domain fragments of CaBP1: N-domain (residues 1–91) and C-domain (96–167). The ^{1}H-^{15}N-HSQC spectra of the domain constructs (Fig. 2, *B* and *C*) indicate that each domain is separately folded without having the other domain present. In addition, the backbone amide chemical shifts for each residue in the domain fragments are nearly identical to the corresponding chemical shifts of the full-length protein. Thus, the structures of the isolated domain fragments must remain intact in the full-length protein, consistent with two non-interacting domains.

On the basis of our NMR analyses above, CaBP1 has two independently folded domains (N-domain, EF1 and EF2, and C-domain, EF3 and EF4) separated by a flexible linker. The structures of each domain were analyzed separately below. The C-domain structure was solved by analyzing NMR spectra of a peptide fragment (CaBP1-C, residues, 96–167), whereas the structure of the Mg^{2+}-bound N-domain was solved by analyzing NMR spectra of full-length CaBP1. The Ca^{2+}-bound N-domain was not studied because it does not bind Ca^{2+} under physiological conditions (28). In summary, we present below three separate NMR solution structures of CaBP1: 1) Mg^{2+}-bound N-domain (PDB 2k7b), 2) Mg^{2+}-bound C-domain (PDB 2k7c), and 3) Ca^{2+}-bound C-domain (PDB 2k7d). The statistics for these structures are summarized in Table 1.

Structure of Mg^{2+}-bound CaBP1—The first 21 N-terminal residues of CaBP1 exhibited weak NMR intensities and could not be accurately analyzed. The remaining residues (22–167) exhibited strong ^{1}H-^{15}N-HSQC peaks and their sequence-specific NMR assignments were analyzed and described previously (36) (BMRB number 15197). The assigned resonances in the HSQC spectrum represent main chain and side chain amide groups that serve as fingerprints of the overall conformation. Three-dimensional protein structures derived from the NMR assignments were calculated on the basis of NOE data, slowly exchanging amide NH groups, chemical shift analysis, and $^3J_{NH\alpha}$ spin-spin coupling constants (see "Experimental Procedures"). The final NMR-derived structures of Mg^{2+}-bound CaBP1 are illustrated in Fig. 3, *A* and *B*.

The Mg^{2+}-bound CaBP1 structure contains a total of eight α-helices and four β-strands: α1 (residues 22–34), α2 (residues 44–54), α3 (residues 61–70), α4 (residues 80–88), α5 (residues 101–111), α6 (121–130), α7 (residues 140–147), α8 (residues 158–165), β1 (residues 41–43), β2 (residues 77–79), β3 (residues 118–120), and β4 (residues 155–157) (Fig. 1). CaBP1 contains two domains comprising four EF-hands (Fig. 3): EF1 (*green*, residues 26–55) and EF2 (*red*, residues 62–91)) are linked and form the N-domain; likewise, EF3 (*cyan*, residues 103–132) and EF4 (*yellow*, residues 140–169) form the C-domain. The two domains do not interact structurally (Fig. 2). Each EF-hand consists of a helix turn helix structure similar to the closed structure of Ca^{2+}-free EF-hands seen in previous structures of apo-CaM (45–47) and troponin C (48). The interhelical angles for the EF-hands are 126.8° (EF1), 140.2° (EF2), 140.1° (EF3), and 126.2° (EF4) (see Table 2). The overall main chain structures of Mg^{2+}-bound N-domain (Fig. 3*A*) and C-domain (Fig. 3*B*) are very similar to those of apo-CaM. The root mean square deviation is 1.5 and 1.3 Å when comparing the main chain atoms of Mg^{2+}-bound CaBP1 with those of apo-CaM in the N-domain and C-domain, respectively.

The NMR structure of Mg^{2+}-bound CaBP1 indicates that Mg^{2+} is bound at EF1 as evidenced by Mg^{2+}-dependent amide chemical shift changes for residues in the EF1 binding loop (Asp^{35}, Asp^{37}, Asp^{39}, and Gly^{40}). Mg^{2+}-binding caused a large downfield amide proton chemical shift for Gly^{40} due in part to formation of a strong hydrogen bond between its main chain amide proton and the carboxylate side chain of Asp^{35}. To identify possible chelating interactions with the bound Mg^{2+}, we made the following point mutations (D35A, D37A, D39A, and D46A) to residues in the EF1 loop at positions 1, 3, 5, and 12. Mg^{2+} binding to each mutant *versus* wild type was monitored by analyzing the Gly^{40} amide resonance. The Mg^{2+}-binding analysis revealed that Asp^{35}, Asp^{37}, and Asp^{39} are each essential for high affinity Mg^{2+} binding, suggesting that their carboxy-

late side chains might form coordinate covalent bonds with the bound Mg^{2+}. A similar Mg^{2+} binding geometry involving acidic side chains from residues at positions 1, 3, and 5 was also observed in the structure of Mg^{2+}-bound calbindin (49). The stereochemical geometry and chelation of the bound Mg^{2+} at EF1 (*magenta sphere*, Fig. 3*A*) was modeled like that described by Ref. 50. The EF2 loop in CaBP1 does not bind Ca^{2+} or Mg^{2+} and is structurally distorted by the presence of Gly^{75} at the fifth position in the binding loop.

Structure of Ca^{2+}-bound CaBP1—The NMR-derived structure of the Ca^{2+}-bound CaBP1-C is shown in Fig. 3*C* (37) (BMRB number 15623). The secondary structure of Ca^{2+}-bound CaBP1 is nearly identical to that determined above for Mg^{2+}-bound CaBP1 (Fig. 1). By contrast, the overall tertiary structure of Ca^{2+}-bound CaBP1-C (Fig. 3*C*) is quite different from that of Mg^{2+}-bound CaBP-C (Fig. 3*B*), reminiscent of the Ca^{2+}-induced closed to open transition seen previously in CaM (45) and troponin C (48). The structures of EF3 and EF4 in Ca^{2+}-bound CaBP1 resemble the familiar "open" conformation of Ca^{2+} occupied EF-hands in CaM (27) and many other EF-hand proteins. The interhelical angles are 100.6° (EF3) and 110.6° (EF4) for Ca^{2+}-bound CaBP1 (see Table 2). The overall main chain structure of Ca^{2+}-bound CaBP1-C (Fig. 3*C*) is very similar to that of Ca^{2+}-bound CaM with a root mean square deviation is 1.2 Å when comparing their main chain atoms.

The NMR structure of Ca^{2+}-bound CaBP1 confirms Ca^{2+} binding at EF3 and EF4, as evidenced by characteristic Ca^{2+}-dependent amide chemical shift changes assigned to Gly^{117} in EF3 and Gly^{154} in EF4. Ca^{2+}-binding caused large downfield amide proton chemical shifts for Gly^{117} and Gly^{154} due in part to formation of a strong hydrogen bond between its main chain amide proton and the carboxylate side chain of Asp^{112} (EF3) and

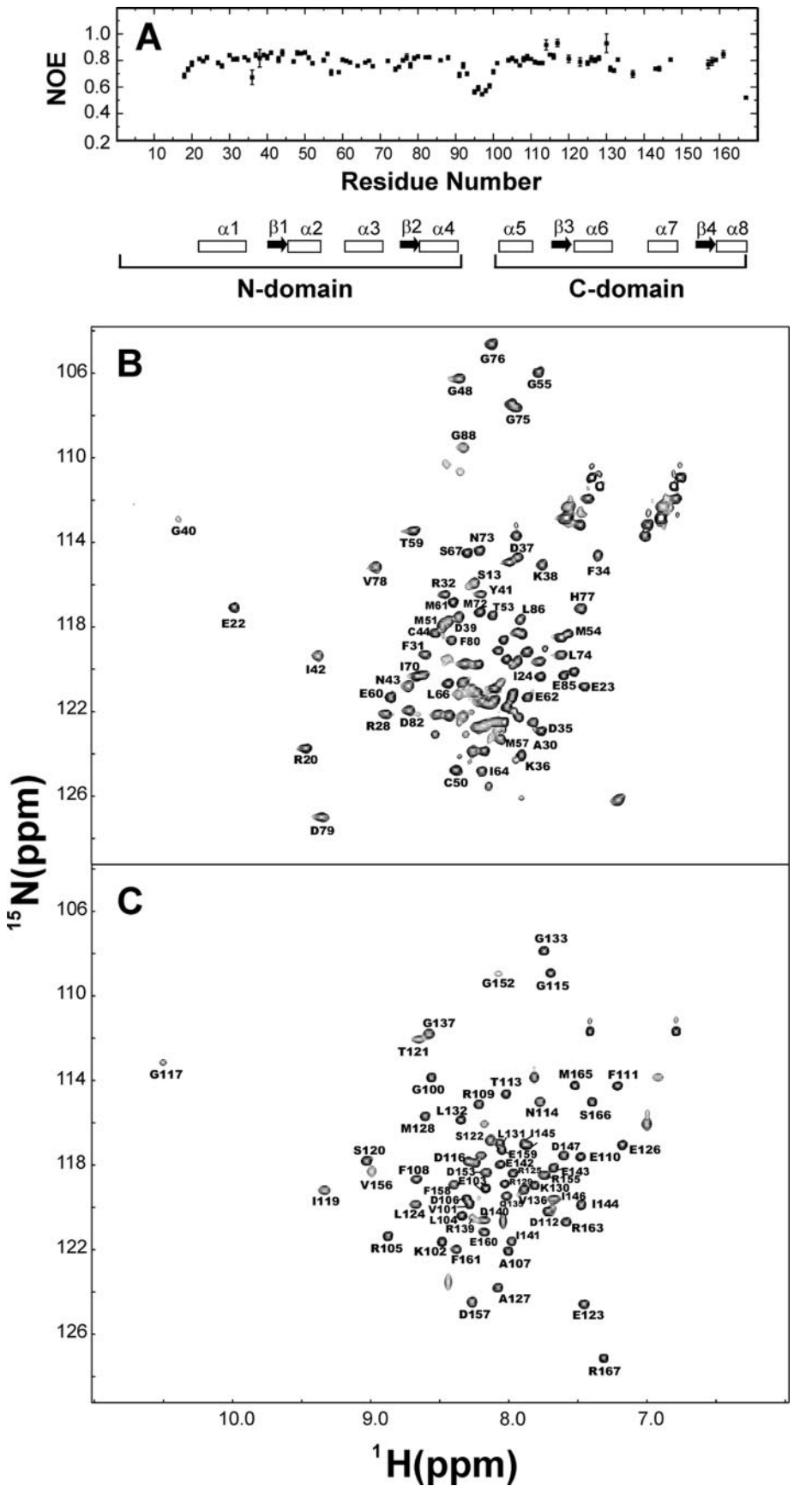

FIGURE 2. **{^{1}H}-^{15}N NOE data for Mg^{2+} bound CaBP1 (*A*) and ^{15}N-^{1}H-HSQC spectra of Mg^{2+}-bound CaBP1-N (*B*) and CaBP1-C (*C*).** A schematic representation of the secondary structure is shown at the bottom in *A* with α-helices and β-strands indicated by *boxes* and *arrows*, respectively.

TABLE 1
Structural statistics for the ensemble structures of CaBP1

	Mg^{2+}-bound N-domain	Mg^{2+}-bound C-domain	Ca^{2+}-bound C-domain
NOE restraints	874	795	814
Intra (|i-j| = 0)	198	284	324
Medium (0<|i-j|≤4)	473	338	309
Long (|i-j|>4)	203	173	181
Hydrogen bonds restraints	56	50	50
Dihedral angle restraints (ϕ,ψ)	96	88	88
Root mean square deviation from ideal geometry			
Bond length (Å)	0.0069 ± 0.0001	0.0068 ± 0.0003	0.0065 ± 0.0001
Bond angle (deg)	1.87 ± 0.008	1.87 ± 0.007	1.83 ± 0.0007
Root mean square deviation from average structure (Å)			
Secondary structure (backbone)	0.58 ± 0.14	0.47 ± 0.09	0.51 ± 0.10
Secondary structure (heavy)	1.22 ± 0.10	1.33 ± 0.11	1.30 ± 0.10
Ramachandran plot (%)			
Most favored region	73.8	77.4	79.4
Allowed region	26.1	21.6	19.8
Disallowed region	0.0	1.0	0.8
Average energy (kcal mol^{-1})			
Total	1359.3	1217.4	1190.8
Distance	61.5	47.7	35.3

Asp^{149} (EF4), respectively. The geometry of the coordinate covalent bonds formed between chelating amino acid residues in CaBP1 and the bound Ca^{2+} could not be observed directly in our NMR study. Instead, the stereochemical geometry and chelation of Ca^{2+} bound at EF3 and EF4 (*orange spheres*, Fig. 3*C*) was modeled using structural constraints derived from the x-ray crystal structure of Ca^{2+}-bound CaM (27), which closely resembles the binding site geometry conserved in other EF-hand proteins (51).

Dimerization of CaBP1?—Previous hydrodynamic analyses of CaBP1 suggested a monomer-dimer equilibrium under NMR conditions (28). Indeed, our ^{15}N NMR relaxation analysis (T_1 and T_2) of CaBP1 in this study suggests an average rotational correlation time of ~12 ns (consistent with a protein dimer) that decreased somewhat when the protein concentration was lowered 10-fold. But, we did not observe any significant chemical shift changes in NMR spectra recorded as a function of protein concentration (50 μM to 1 mM). Also, intermolecular NOEs could not be detected in ^{13}C-filtered NOESY-HMQC spectra of CaBP1 recorded from a mixed labeled sample. Thus, the CaBP1 monomer-dimer equilibrium must have an exchange rate that is much faster than the chemical shift time scale and the structure of the dimer cannot be resolved by NMR. Such fast exchange kinetics and hence low affinity for dimerization (K_d ~ 100 μM) is not likely to be physiologically relevant and was not characterized further.

Surface Properties of CaBP1 Versus CaM—Space filling representations of Mg^{2+}-bound and Ca^{2+}-bound CaBP1 are illustrated and compared with those of CaM (Fig. 4). The surface residues of Mg^{2+}-bound CaBP1 are similar to those of apo-CaM (Fig. 4, *A* and *B*). The N-domain of Mg^{2+}-bound CaBP1 contains mostly negatively charged residues on the protein surface (*highlighted red* in Fig. 4*A*) that remain invariant in CaM, and the overall surface charge is nearly the same between the two. The C-domain surface of Mg^{2+}-bound CaBP1 also looks similar to that of apo-CaM (Fig. 4*B*). The N-domain has a few exposed hydrophobic residues in Mg^{2+}-bound CaBP1 (Met^{57}, Met^{61}, Met^{72}, and Leu^{74}) not conserved in CaM (Fig. 1) that might serve a functional role in target recognition.

The protein surface of Ca^{2+}-bound CaBP1-C is somewhat different from that of Ca^{2+}-bound CaM (Fig. 4*C*). The front face of Ca^{2+}-bound CaBP1-C exhibits a striking solvent-exposed hydrophobic surface (*highlighted yellow* in Fig. 4*C*) that is wider and more expansive than that of Ca^{2+}-bound CaM. The solvent-exposed hydrophobic patch in Ca^{2+}-bound CaBP1-C contains non-conserved residues located in the loop between EF3 and EF4 (Leu^{132}, His^{134}, Val^{136}, and His^{138}), the helix of EF4 (Ile^{141}, Ile^{144}, and Val^{148}), and the domain linker (Ile^{99} and Val^{101}). The exposed hydrophobic patch is surrounded by a ring of charged residues that might form electrostatic contacts with target proteins. Basic residues in CaBP1 (Lys^{102}, His^{134}, His^{138}, and Arg^{139}) are replaced by negatively charged residues in CaM that might confer specific electrostatic contacts. We suggest that these nonconserved residues on the surface of Ca^{2+}-bound CaBP1 may form a target binding site and help explain the highly selective binding of CaBP1 to InsP$_3$Rs.

CaBP1 Interaction with N-terminal Cytosolic Residues in InsP$_3$R1—CaBP1 was shown previously to regulate Ca^{2+}-induced channel activity of InsP$_3$Rs and the CaBP1 interaction site was localized to the N-terminal cytosolic region of InsP$_3$R1 (residues 1–604) (13). We performed a series of target binding studies using isothermal titration calorimetry (ITC) and NMR to characterize the structural interaction between CaBP1 and InsP$_3$R1 (Fig. 5). An N-terminal peptide fragment of InsP$_3$R1 (residues, 1–587, called InsP$_3$R-(1–587)), saturated with InsP$_3$, exhibited strongly exothermic binding ($\Delta H = -1.96$ kcal/mol) to Ca^{2+}-bound CaBP1 with a 1:1 stoichiometry and a dissociation constant (K_d) of 3 μM (Fig. 5*A*). By contrast, InsP$_3$R-(1–587) exhibited about 10-fold weaker binding to Mg^{2+}-bound CaBP1 ($\Delta H = -1.55$ kcal/mol and $K_d = 30$ μM). InsP$_3$R-(1–587) showed no detectable binding to either Ca^{2+}-free or Ca^{2+}-bound CaM under these same conditions, which was somewhat surprising given that Ca^{2+}-CaM has been suggested to bind InsP$_3$R1 and negatively regulate channel gating (12). Also, apo-InsP$_3$R-(1–587) binds to CaBP1 with approximately the same affinity as the ligand-bound receptor. Thus, ligand-bound InsP$_3$R-(1–587) exhibits Ca^{2+}-induced binding to CaBP1 with high selectivity over CaM.

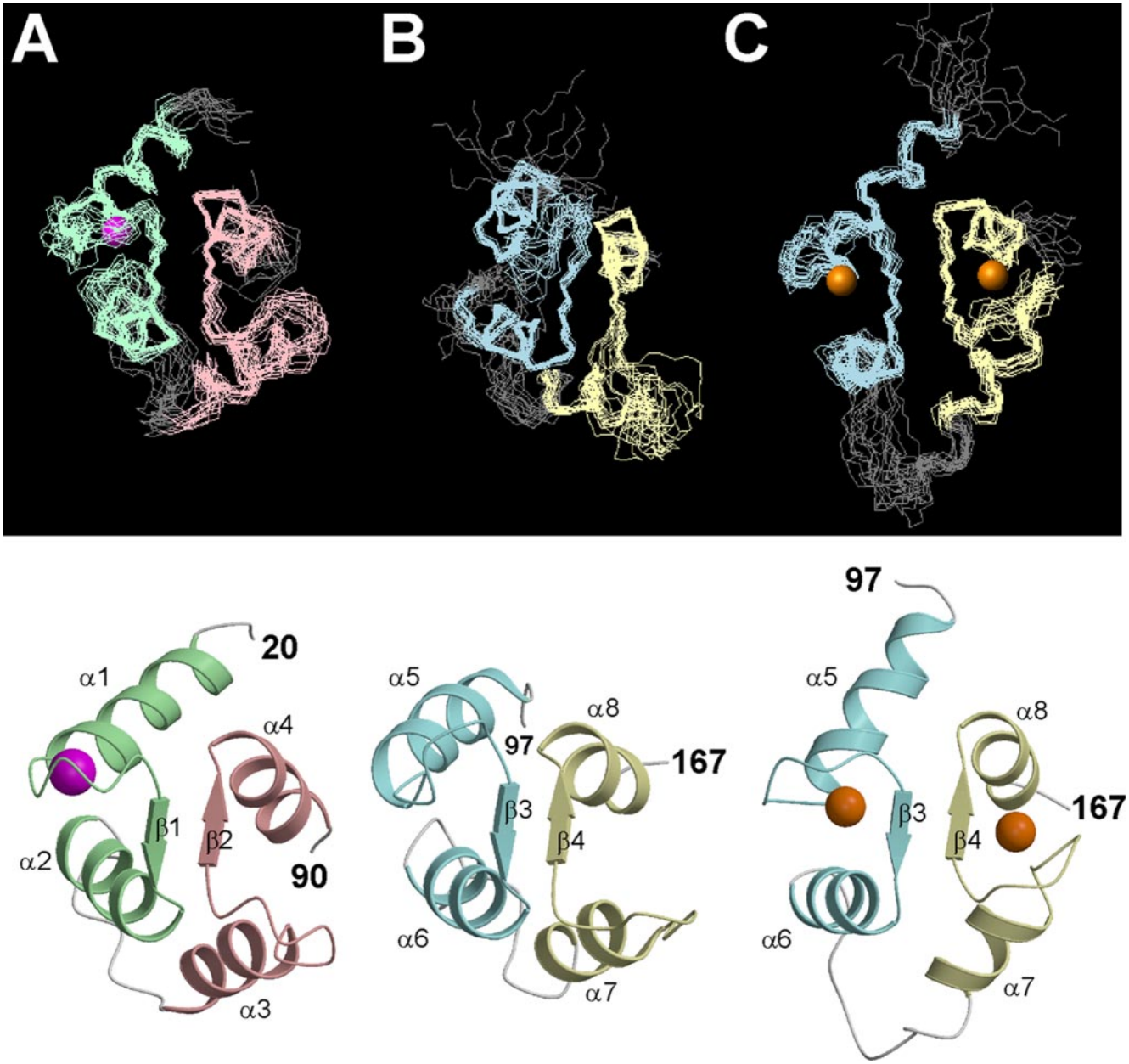

FIGURE 3. **Main chain structures of CaBP1 determined by NMR.** Superposition of the 15 lowest energy structures (*top*) and ribbon representations of the energy-minimized average structure (*bottom*) are illustrated for: *A*, Mg^{2+}-bound N-domain (PDB 2k7b); *B*, Mg^{2+}-bound C-domain (PDB 2k7c); and *C*, Ca^{2+}-bound C-domain (PDB 2k7d). N-terminal residues (1–21) are unstructured and not shown. EF-hands are highlighted in colors as defined in the legend to Fig. 1. *Orange* and *magenta spheres* represent bound Ca^{2+} and Mg^{2+}.

TABLE 2
Interhelical angles of the EF-hands in CaM and CaBP1
Residues in the helices are shown below.

Helix pair	Interhelical angles			
	Apo-CaM[a]	Ca^{2+}-bound CaM[b]	Mg^{2+}-bound CaBP1[c]	Ca^{2+}-bound CaBP1[c]
	degree			
α_1-α_2	130.9	103.8	126.8	
α_3-α_4	130.8	101.0	140.2	
α_5-α_6	139.5	101.0	140.1	100.6
α_7-α_8	126.0	101.0	126.2	110.6

[a] Apo-CaM (PDB accession code 1dmo): (a1) 6–18, (a2) 29–38, (a3) 45–55, (a4) 65–75, (a5) 82–90, (a6) 103–112, (a7)118–127, (a8) 137–143.
[b] Ca^{2+} bound CaM (PDB accession code 1j7p): (a1) 6–19, (a2) 29–38, (a3) 45–55, (a4) 65–75, (a5) 83–92, (a6) 102–111, (a7)118–128, (a8) 138–145.
[c] CaBP1: (a_1) 22–34, (a_2) 45–54, (a_3) 61–70, (a_4) 80–88, (a_5) 101–110, (a_6) 121–130, (a_7) 141–147, (a_8)158–165.

The lack of $InsP_3R$-(1–587) binding to CaM was also verified by using NMR in which the ^1H-^{15}N-HSQC spectrum of ^{15}N-labeled CaM remained unaffected as a function of adding excess, unlabeled $InsP_3R$-(1–587). The ^1H-^{15}N-HSQC spectrum of ^{15}N-labeled CaBP1, by contrast, exhibited striking peak broadening and chemical shift changes upon addition of saturating $InsP_3R$-(1–587), further demonstrating that CaBP1 binds to $InsP_3R$-(1–587). Unfortunately, because all NMR peaks in the HSQC spectrum of CaBP1 are severely broadened and uniformly affected by $InsP_3R$-(1–587) binding, it was not possible to identify any specific binding site residues by chemical shift mapping.

The $InsP_3R1$-binding site on CaBP1 was investigated by performing ITC experiments separately on N-domain and C-do-

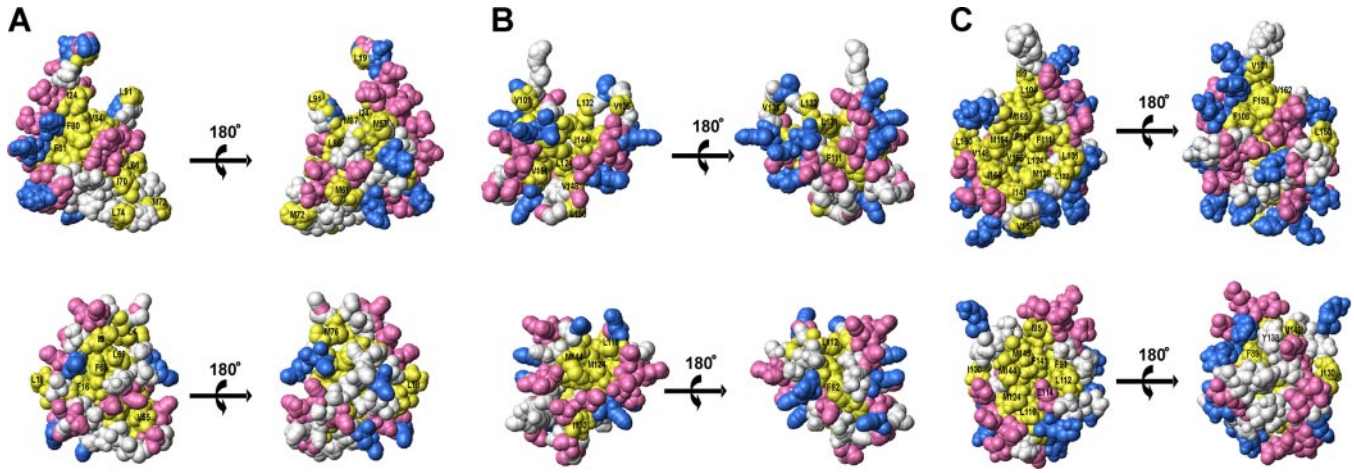

FIGURE 4. **Space-filling representation of CaBP1 (*top*) and CaM (*bottom*) illustrating (*A*) Mg^{2+}-bound N-domain of CaBP1 (PDB 2k7b) and apo-CaM (PDB 1dmo), (*B*) Mg^{2+}-bound C-domain of CaBP1 (PDB 2k7c) and apo-CaM (PDB 1dmo), and (*C*) Ca^{2+}-bound C-domain of CaBP1 (PDB 2k7d) and Ca^{2+}-CaM (PDB 1j7p).** Acidic residues (Asp and Glu), basic residues (Arg, His, Lys), and hydrophobic residues (Ile, Leu, Phe, Trp, Val) are colored *red*, *blue*, and *yellow*, respectively.

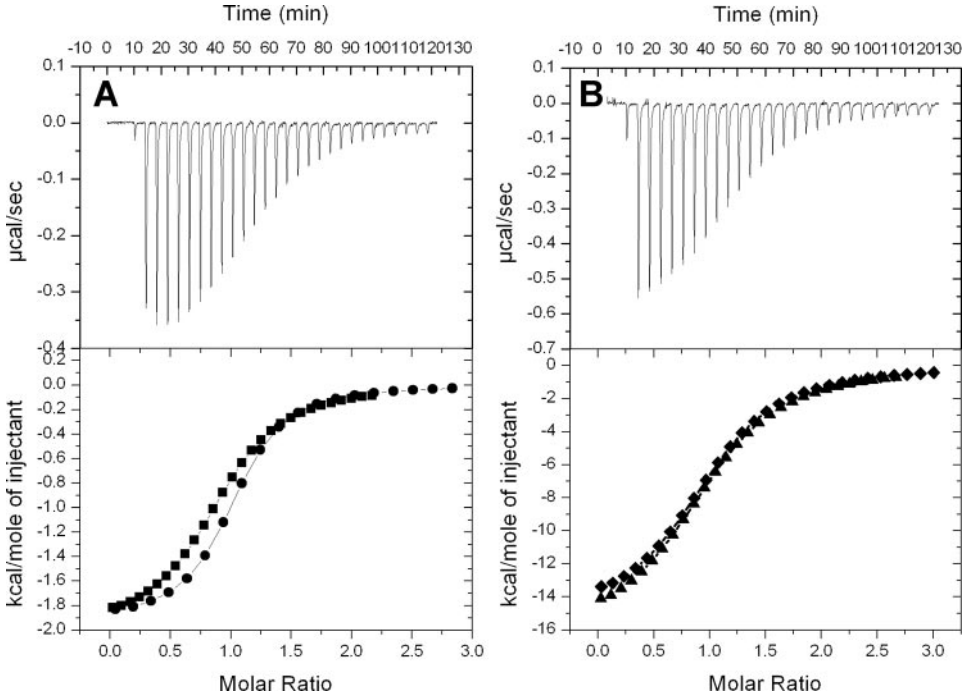

FIGURE 5. **Isothermal titration microcalorimeteric analysis for the binding of $InsP_3R1$-(1–587) to (*A*) Ca^{2+}-bound CaBP1 and (*B*) $InsP_3$.** Experimental traces of the calorimetric titration (25 × 10-µl aliquots) are shown in the *top panel* and the intergrated binding isotherms are shown in the *bottom panel*. Binding data are overlaid in the bottom panels for the binding of $InsP_3R$-(1–587) to (*A*) full-length CaBP1 (*squares*) and CaBP1-C (*circles*) and (*B*) $InsP_3$ in the presence (*diamonds*) or absence (*triangles*) of CaBP1. The binding isotherms were fit to a one-site model and fitting parameters are reported in Table 3.

main fragments of CaBP1 (CaBP1-N and CaBP1-C). $InsP_3R$-(1–587) binds to CaBP1-C with nearly the same enthalpy ($\Delta H = -1.92$ kcal/mol), dissociation constant ($K_d = \sim 2\ \mu$M), and Ca^{2+} dependence as seen above for binding to full-length CaBP1 (Fig. 5*A*). By contrast, $InsP_3R$-(1–587) failed to exhibit any detectable binding to CaBP1-N by ITC. The lack of such binding was verified under NMR conditions wherein the ^{1}H-^{15}N-HSQC spectrum of ^{15}N-labeled CaBP1-N did not change as a function of adding excess $InsP_3R$-(1–587). ^{1}H-^{15}N-HSQC spectra of ^{15}N-labeled CaBP1-C changed dramatically upon adding saturating $InsP_3R$-(1–587) similar to that described above for full-length CaBP1. Thus, $InsP_3R$-(1–587) binds selectively to Ca^{2+}-bound CaBP1-C and does not interact with CaBP1-N.

To probe the CaBP1-binding site within $InsP_3R$-(1–587), ITC studies were performed separately by using the suppressor domain (residues 1–224, $InsP_3R_{sup}$) and the $InsP_3$ binding core domain (residues 236–604, $InsP_3R_{core}$). No heat signal could be detected upon individually adding either the suppressor domain and/or core domain to CaBP1, suggesting either $\Delta H = 0$ or a lack of binding in the micromolar range ($K_d \gg 10^{-4}$ M). A lack of binding under NMR conditions was verified by the ^{1}H-^{15}N-HSQC spectrum of ^{15}N-labeled CaBP1 (full-length) that remained unaffected as a function of adding excess suppressor and/or core domain. Thus, CaBP1 does not exhibit high affinity binding to either the suppressor or core domain alone, but rather the two domains must be linked together to have high affinity binding to CaBP1.

The binding of CaBP1 to $InsP_3R$-(1–587) has little or no effect on ligand-binding affinity. The binding of $InsP_3$ to $InsP_3R$-(1–587) is exothermic ($\Delta H = -16.2$ kcal/mol) with a 1:1 stoichiometry and dissociation constant (K_d) of ~1 µM (Fig. 5*B*). The apparent K_d measured by ITC is at least 100-fold weaker than the intrinsic ligand binding affinity measured for full-length $InsP_3R1$ (52). The discrepancy could be explained in part by a protein conformational change in $InsP_3R$-(1–587) coupled to $InsP_3$ binding. The intrinsic binding of $InsP_3$ ($K_a \sim 10^8\ M^{-1}$) if coupled to an unfavorable conformational change

($K_{eq} \sim 10^{-2}$) would yield an overall equilibrium constant of $K_{tot} = K_a \times K_{eq} \sim 10^6\ M^{-1}$, consistent with the overall K_d measured by ITC. Thus, $InsP_3$ binding to $InsP_3R$-(1–587) induces a protein conformational change, consistent with predictions from small-angle x-ray scattering analysis (35). The apparent K_d for $InsP_3$ binding to $InsP_3R$-(1–587) is NOT affected by the presence or absence of saturating CaBP1 (Fig. 5*B*), demonstrating that CaBP1 binding to $InsP_3R$-(1–587) does not block or otherwise influence ligand binding.

Structural Model of the CaBP1·$InsP_3R$-(1–587) Complex—The relatively low solubility of the CaBP1·$InsP_3R$-(1–587) complex has thus far hampered our efforts to directly solve the complex structure by NMR or x-ray crystallography. Instead, we used a computational docking approach that takes into account variables such as shape complementarity, desolvation energetics, and electrostatics to simulate the structure of the protein complex (53). Separate x-ray crystal structures have been solved recently for $InsP_3R_{sup}$ (54) and $InsP_3R_{core}$ (55). Our ITC analysis indicates that CaBP1-C binds cooperatively to $InsP_3R_{sup}$ and $InsP_3R_{core}$ only when both domains are connected (Fig. 5). This cooperativity suggests that CaBP1-C might contact both $InsP_3R_{sup}$ and $InsP_3R_{core}$ in the complex. The first step in the model calculation was to individually dock CaBP1-C to each domain and generate binary complexes: CaBP1-C·$InsP_3R_{sup}$ and CaBP1-C·$InsP_3R_{core}$. Structures of the separate binary complexes were then aligned with respect to CaBP1-C to predict the disposition of $InsP_3R_{sup}$ and $InsP_3R_{core}$ in the ternary complex.

A total of 20 independent docking calculations were performed for each binary complex. A statistical analysis of the CaBP1-$InsP_3R_{sup}$ docked structures revealed a striking tendency for CaBP1-C to bind to an exposed surface on the helical "arm" (residues 66–110) in $InsP_3R_{sup}$, suggested previously to be functionally important (14, 56). This docking model is also consistent with previous mutagenesis studies, suggesting that the arm residues interact with $InsP_3R_{core}$ (55). Arm residues (66–81) also form a potential calmodulin binding motif shown previously to inhibit CaBP1 binding to $InsP_3R1$ (14). Finally, it is well known that EF-hand proteins generally bind to helical segments in target proteins (57). Thus, the docking interactions of CaBP1-C with the suppressor helical arm are plausible and well justified experimentally. The family of docked structures of the CaBP1·$InsP_3R_{core}$ complex revealed a tendency for CaBP1-C to interact with the β-trefoil subdomain (residues 397–420) located on the opposite face from the ligand-binding site. The lowest energy structures of the CaBP1·$InsP_3R_{sup}$ and CaBP1·$InsP_3R_{core}$ binary complexes were then aligned with respect to CaBP1. Candidate docked structures were selected that minimize any overlap between $InsP_3R_{sup}$ and $InsP_3R_{core}$ while maintaining a reasonably close distance (<30 Å) between the final residue of $InsP_3R_{sup}$ and initial residue of $InsP_3R_{core}$.

A representative structure of the docked CaBP1·$InsP_3R_{sup}$·$InsP_3R_{core}$ complex is shown in Fig. 6. CaBP1-C interacts primarily with the arm helix in the suppressor domain (residues 72–94, colored *brown* in Fig. 6), suggested previously to interact with CaBP1 (8, 13, 14). This CaBP1-binding site on $InsP_3R1$ is located far away from the ligand binding site, consistent with CaBP1 having no effect on the ligand-binding affinity (Fig. 5*B*).

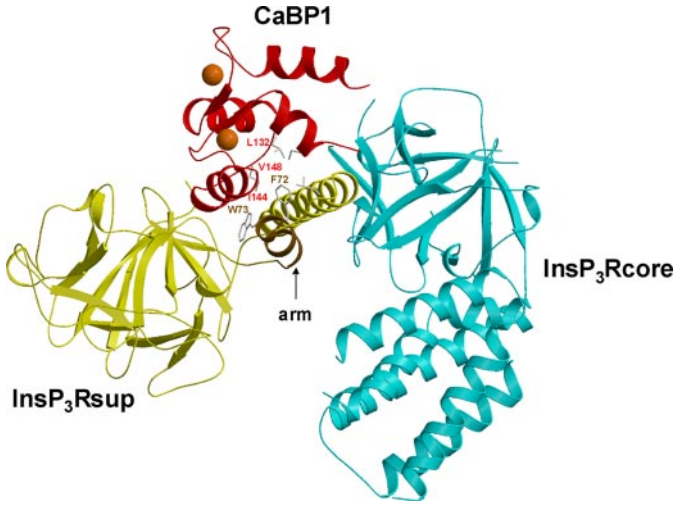

FIGURE 6. **Structural model of the docked complex for CaBP1-C·$InsP_3R_{sup}$/$InsP_3R_{core}$.** CaBP1-C, $InsP_3R_{sup}$ (residues 2–223), and $InsP_3R_{core}$ (residues 236–586) are colored *red*, *yellow*, and *cyan*, respectively. Arm helix of $InsP_3R_{core}$ interacting with CaBP1 is colored *brown*. The docking calculation was performed using Zdock as described under "Experimental Procedures."

TABLE 3

ITC fitting parameters for the binding of $InsP_3R$-(1–587) to various molecules

Molecule	K_d	ΔH	ΔS
	μM	*kcal mol*$^{-1}$	*cal mol*$^{-1}$ *K*$^{-1}$
Mg^{2+}-bound CaBP1	30 ± 3	−1.55 ± 0.1	15.9
Ca^{2+}-bound CaBP1	3 ± 0.3	−1.96 ± 0.2	17.9
Mg^{2+}-bound CaBP1-C	30 ± 3	−0.36 ± 0.1	21.7
Ca^{2+}-bound CaBP1-C	2.5 ± 0.3	−1.92 ± 0.2	19.3
Ca^{2+}-bound CaBP1-C (ΔL132)	3.6 ± 0.3	−2.22 ± 0.2	17.7
Ca^{2+}-bound CaBP1-C (H134E)	5.6 ± 0.5	−2.35 ± 0.2	16.5
Ca^{2+}-bound CaBP1-C (V148A)	5.1 ± 0.4	−2.03 ± 0.2	17.3
Mg^{2+}-bound CaBP1-N	–[a]	–	–
Ca^{2+}-bound CaBP1-N	–	–	–
Apo-CaM	–	–	–
Ca^{2+}-bound CaM	–	–	–
$InsP_3$	1.9 ± 0.2	−16 ± 0.4	−27.5
$InsP_3$ (+CaBP1)	1.6 ± 0.2	−15 ± 0.6	−24.7

[a] Indicates no detectable binding.

The exposed hydrophobic patch of Ca^{2+}-bound CaBP1-C (Fig. 4*C*) interacts with both arm helices of $InsP_3R_{sup}$. The aromatic rings of Phe^{72} and Trp^{73} (suppressor domain) contact the side chains of Ile^{144}, Val^{148}, and Met^{164} of CaBP1. Also, non-conserved CaBP1 residues (Leu^{132}, His^{134}, and Val^{148} highlighted *red* in Fig. 1) interact with the C-terminal arm helix that might help explain its highly specific binding to CaBP1 *versus* CaM. Indeed, the CaBP1 mutants (ΔL132, H134E, V148A) show ~2-fold weaker binding to $InsP_3$-(1–587) (Table 3). CaBP1 also makes a few contacts with residues in $InsP_3R_{core}$ (residues 405–409) that are also close to $InsP_3R_{sup}$ helical arm residues, which might explain in part the cooperative interaction. Nearly all exposed residues on the C-terminal arm helix (Leu^{88}, Lys^{91}, His^{94}, Ala^{95}, Leu^{98}, and Thr^{105}) interact with exposed β-trefoil residues from $InsP_3R_{core}$, consistent with previous mutagenesis studies (55). The extensive domain interface predicted in Fig. 6 causes $InsP_3R_{sup}$ and $InsP_3R_{core}$ to interact in a relatively compact arrangement, consistent with previous small-angle x-ray scattering measurements on $InsP_3R$-(1–587) (35). We conclude that CaBP1 binding to the receptor may stabilize a structural interaction between $InsP_3R_{sup}$ and $InsP_3R_{core}$ that might play a role in channel gating. This cooperative interdomain associa-

tion appears to reciprocally stabilize the helical arm interaction with CaBP1 and therefore explain why $InsP_3R_{sup}$ and $InsP_3R_{core}$ are both required for high affinity binding by CaBP1.

DISCUSSION

In this study, we determined the NMR solution structures of CaBP1 in both Mg^{2+}-bound and Ca^{2+}-bound states and characterized their structural interaction with $InsP_3R1$. The overall main chain structure of Mg^{2+}-bound CaBP1 (Fig. 3, *A* and *B*) is similar to that seen previously in apo-CaM (45) and troponic C (48). One important difference is that Mg^{2+} is bound tightly at EF1 in CaBP1. The structure of Ca^{2+}-bound CaBP1 is somewhat different from that of CaM (Fig. 4*C*). At saturating Ca^{2+} levels, the CaBP1 N-domain does NOT bind Ca^{2+} but remains in a closed conformation with Mg^{2+} bound at EF1. The C-domain binds Ca^{2+} at EF3 and EF4 and adopts the familiar Ca^{2+}-bound open conformation (Fig. 3*C*) with an exposed hydrophobic patch (Fig. 4*C*). Many of the exposed hydrophobic residues in CaBP1 (Leu^{132}, His^{134}, Ile^{144}, and Val^{148}) are not conserved in CaM and might play a role in controlling the highly specific and Ca^{2+}-induced binding to $InsP_3R1$ to CaBP1 (Fig. 6). Indeed, the CaBP1 mutants (ΔL132, H134E, and V148A) show noticeably weaker binding to $InsP_3$-(1–587) (Table 3).

Our target binding analysis indicates that Ca^{2+}-bound CaBP1 binds tightly to $InsP_3R$-(1–587) but does not bind to either $InsP_3R_{sup}$ or $InsP_3R_{core}$ alone. These observations seem somewhat at odds with an earlier report, suggesting that CaBP1 can bind to isolated segments of $InsP_3R_{sup}$ independent of Ca^{2+} (14). Indeed, such binding of CaBP1 to $InsP_3R_{sup}$ is consistent with our proposed structural model of CaBP1-$InsP_3R$ (Fig. 6), showing that CaBP1 forms intimate contacts with the helical arm in $InsP_3R_{sup}$. However, the affinity of CaBP1 binding to $InsP_3R_{sup}$ alone must be quite low, which would explain why this weak binding escaped detection in our ITC analysis (Fig. 5). Furthermore, we suggest that the affinity of CaBP1 binding to $InsP_3R1$ is significantly enhanced by the cooperative interaction between $InsP_3R_{sup}$ and $InsP_3R_{core}$ as depicted in Fig. 6. This same interaction also appears to partially block the ligand binding site, which may explain why $InsP_3$ binds with ~10-fold higher affinity to an isolated fragment of $InsP_3R_{core}$ than it binds to $InsP_3R1$ (52).

Previous studies have suggested that $InsP_3R1$ binds to both the Ca^{2+}-free and Ca^{2+}-bound forms of CaBP1 (13, 14). In this study, we confirm that $InsP_3R$-(1–587) does indeed bind to both the Mg^{2+}-bound and Ca^{2+}-bound CaBP1. However, our more quantitative ITC analysis reveals that Ca^{2+}-bound CaBP1 binds to $InsP_3R$-(1–587) with ~10-fold higher affinity compared with that of Mg^{2+}-bound CaBP1. Furthermore, the Mg^{2+}-bound CaBP1 N-domain does NOT bind to $InsP_3R$-(1–587) (Table 3). The lower affinity target binding by Mg^{2+}-bound/Ca^{2+}-free CaBP1 (C-domain) at low, basal Ca^{2+} levels might represent its binding to IQ-motifs in the receptor (12). Alternatively, we submit that the 10-fold stronger binding by Ca^{2+}-bound CaBP1 may be sufficient to exclude $InsP_3R1$ binding to Ca^{2+}-free CaBP1 under physiological conditions. Thus, CaBP1 would selectively bind to $InsP_3R1$ only when the cell is stimulated (at high cytosolic Ca^{2+} levels) and modulate Ca^{2+}-dependent channel gating.

$InsP_3R$-(1–587) binds to CaBP1 with at least 100-fold higher affinity than its binding to CaM. The highly selective binding to CaBP1 is explained in part by the large solvent-exposed surface area of the hydrophobic patch in CaBP1-C (Fig. 4*C*) as well as by a number of non-conserved residues on this surface (Fig. 1). Non-conserved CaBP1 residues (Leu^{132}, His^{134}, Ile^{144}, and Val^{148}) are proposed to make unique hydrophobic contacts with the helical arm of $InsP_3R_{sup}$ (Fig. 6). The highly specific binding of $InsP_3R$-(1–587) to CaBP1 relative to CaM illustrates that CaBP1 is a specialized Ca^{2+} sensor for regulating $InsP_3Rs$ in the brain and retina. This contrasts with CaM that is ubiquitously expressed in all tissues and has a much broader range of target interactions. The specialized target binding by CaBP1 may be augmented by CaBP splice variants and isoforms that exhibit tissue-specific neuronal expression (19–21). We propose that the multiplicity of CaBPs in the central nervous system might play a role in fine tuning their interaction with various $InsP_3R$ isoforms and other Ca^{2+} channel targets.

CaBP1 has been suggested to promote channel opening in the absence of $InsP_3$ (13). CaBP1 binds to $InsP_3R$-(1–587) both in the presence or absence of $InsP_3$, and CaBP1 has little or no effect on $InsP_3$ binding to $InsP_3R$-(1–587) (Fig. 5). Thus, CaBP1 interacts structurally with $InsP_3R1$ even in the absence of $InsP_3$. This is consistent with our docking analysis in which CaBP1-C interacts primarily with the helical arm region of the suppressor domain (Fig. 6), located far from the ligand-binding site. It is also possible that CaBP1 binding to apo-$InsP_3R1$ induces structural interactions between $InsP_3R_{sup}$ and $InsP_3R_{core}$ that may mimic structural changes caused by ligand-binding and thus explain the observed $InsP_3$-independent channel opening.

Last, our structural studies suggest that the CaBP1 C-domain alone might be sufficient for promoting Ca^{2+}-dependent channel activity because CaBP1-N does not bind to $InsP_3R$-(1–587). However, the current study does not preclude the CaBP1 N-domain from interacting elsewhere in the channel. For example, Ca^{2+}-dependent inactivation of L-type channels was shown recently to require separate binding by both the N-domain and C-domain of CaM (58). A similar bipartite interaction by the two domains of CaBP1 might also be important for regulation of $InsP_3R1$. The CaBP1 N-domain might bind to either the central regulatory domain or the C-terminal cytosolic domain of $InsP_3R1$. In the future, we plan to further investigate the functional interactions between $InsP_3R1$ and CaBP1 by determining the atomic resolution structure of CaBP1/$InsP_3R$-(1–587) and by exploring a possible role for the CaBP1 N-domain.

Acknowledgments—We are grateful to Dr. Jeff de Ropp for help with NMR experiments, Dr. Frits Abildgaard for providing NMR pulse-sequence programs, and Frank Delaglio for writing computer software for NMR data processing and analysis.

REFERENCES

1. Berridge, M. J. (2003) *Nat. Rev. Mol. Cell. Biol.* **4,** 517–529
2. Berridge, M. J. (1993) *Nature* **361,** 315–325
3. Iino, M. (1990) *J. Gen. Physiol.* **95,** 1103–1122
4. Taylor, C. W., and Laude, A. J. (2002) *Cell Calcium* **32,** 321–334

5. Finch, E. A., Turner, T. J., and Goldin, S. M. (1991) *Science* **252,** 443–446
6. Missiaen, L., Parys, J. B., Weidema, A. F., Sipma, H., Vanlingen, S., De Smedt, P., Callewaert, G., and De Smedt, H. (1999) *J. Biol. Chem.* **274,** 13748–13751
7. Berridge, M. J. (2002) *Cell Calcium* **32,** 235–249
8. Devogelaere, B., Verbert, L., Parys, J. B., Missiaen, L., and De Smedt, H. (2008) *Cell Calcium* **43,** 17–27
9. Foskett, J. K., White, C., Cheung, K. H., and Mak, D. O. (2007) *Physiol. Rev.* **87,** 593–658
10. Sienaert, I., Missiaen, L., De Smedt, H., Parys, J. B., Sipma, H., and Casteels, R. (1997) *J. Biol. Chem.* **272,** 25899–25906
11. Adkins, C. E., Morris, S. A., De Smedt, H., Sienaert, I., Torok, K., and Taylor, C. W. (2000) *Biochem. J.* **345,** 357–363
12. Michikawa, T., Hirota, J., Kawano, S., Hiraoka, M., Yamada, M., Furuichi, T., and Mikoshiba, K. (1999) *Neuron* **23,** 799–808
13. Yang, J., McBride, S., Mak, D. O., Vardi, N., Palczewski, K., Haeseleer, F., and Foskett, J. K. (2002) *Proc. Natl. Acad. Sci. U. S. A* **99,** 7711–7716
14. Kasri, N. N., Holmes, A. M., Bultynck, G., Parys, J. B., Bootman, M. D., Rietdorf, K., Missiaen, L., McDonald, F., De Smedt, H., Conway, S. J., Holmes, A. B., Berridge, M. J., and Roderick, H. L. (2004) *EMBO J.* **23,** 312–321
15. White, C., Yang, J., Monteiro, M. J., and Foskett, J. K. (2006) *J. Biol. Chem.* **281,** 20825–20833
16. Schlecker, C., Boehmerle, W., Jeromin, A., DeGray, B., Varshney, A., Sharma, Y., and Ehrlich, B. E. (2006) *J. Clin. Investig.* **116,** 1668–1674
17. Haeseleer, F., Sokal, I., Verlinde, C. L., Erdjument, H., Tempst, P., Pronin, A. N., Benovic, J. L., Fariss, R. N., and Palczewski, K. (2000) *J. Biol. Chem.* **275,** 1247–1260
18. Ikura, M. (1996) *Trends Biochem. Sci.* **21,** 14–17
19. Haynes, L. P., Tepikin, A. V., and Burgoyne, R. D. (2004) *J. Biol. Chem.* **279,** 547–555
20. Menger, N., Seidenbecher, C. I., Gundelfinger, E. D., and Kreutz, M. R. (1999) *Cell Tissue Res.* **298,** 21–32
21. Seidenbecher, C. I., Reissner, C., and Kreutz, M. R. (2002) *Adv. Exp. Med. Biol.* **514,** 451–463
22. Laube, G., Seidenbecher, C. I., Richter, K., Dieterich, D. C., Hoffmann, B., Landwehr, M., Smalla, K. H., Winter, C., Bockers, T. M., Wolf, G., Gundelfinger, E. D., and Kreutz, M. R. (2002) *Mol. Cell Neurosci.* **19,** 459–475
23. Lee, A., Westenbroek, R. E., Haeseleer, F., Palczewski, K., Scheuer, T., and Catterall, W. A. (2002) *Nat. Neurosci.* **5,** 210–217
24. Zhou, H., Yu, K., McCoy, K. L., and Lee, A. (2005) *J. Biol. Chem.* **280,** 29612–29619
25. Kinoshita-Kawada, M., Tang, J., Xiao, R., Kaneko, S., Foskett, J. K., and Zhu, M. X. (2005) *Pflugers Arch.* **450,** 345–354
26. Haeseleer, F., Imanishi, Y., Maeda, T., Possin, D. E., Maeda, A., Lee, A., Reike, F., and Palczewski, K. (2004) *Nat. Neurosci.* **7,** 1079–1087
27. Babu, Y. S., Bugg, C. E., and Cook, W. J. (1988) *J. Mol. Biol.* **204,** 191–204
28. Wingard, J. N., Chan, J., Bosanac, I., Haeseleer, F., Palczewski, K., Ikura, M., and Ames, J. B. (2005) *J. Biol. Chem.* **280,** 37461–37470
29. Brocard, J. B., Rajdev, S., and Reynolds, I. J. (1993) *Neuron* **11,** 751–757
30. Osawa, M., Dace, A., Tong, K. I., Valiveti, A., Ikura, M., and Ames, J. B. (2005) *J. Biol. Chem.* **280,** 18008–18014
31. Yamniuk, A. P., Nguyen, L. T., Hoang, T. T., and Vogel, H. J. (2004) *Biochemistry* **43,** 2558–2568
32. Cox, J. A., Durussel, I., Comte, M., Nef, S., Nef, P., Lenz, S. E., and Gundelfinger, E. D. (1994) *J. Biol. Chem.* **269,** 32807–32813
33. Schug, Z. T., and Joseph, S. K. (2006) *J. Biol. Chem.* **281,** 24431–24440
34. Varnai, P., Balla, A., Hunyady, L., and Balla, T. (2005) *Proc. Natl. Acad. Sci. U. S. A* **102,** 7859–7864
35. Chan, J., Whitten, A. E., Jefferies, C. M., Bosanac, I., Mal, T. K., Ito, J., Porumb, H., Michikawa, T., Mikoshiba, K., Trewhella, J., and Ikura, M. (2007) *J. Mol. Biol.* **373,** 1269–1280
36. Li, C., and Ames, J. B. (2007) *Biomol. NMR Assign.* **1,** 77–79
37. Li, C., and Ames, J. B. (2008) *Biomol. NMR Assign.* **2,** 61–63
38. Schwieters, C. D., Kuszewski, J. J., Tjandra, N., and Clore, G. M. (2003) *J. Biol. Chem.* **278,** 37461–37470
39. Badger, J., Kumar, R. A., Yip, P., and Szalma, S. (1999) *Proteins* **35,** 25–33
40. Finley, N. L., Howarth, J. W., and Rosevear, P. R. (2004) *Biochemistry* **43,** 11371–11379
41. Chen, R., Li, L., and Weng, Z. (2003) *Protens* **52,** 80–87
42. Chang, S. L., Szabo, A., and Tjandra, N. (2003) *J. Am. Chem. Soc.* **125,** 11379–11384
43. Bourne, Y., Dannenberg, J., Pollmann, V. V., Marchot, P., and Pongs, O. (2001) *J. Biol. Chem.* **276,** 11949–11955
44. Gentry, H. R., Singer, A. U., Betts, L., Yang, C., Ferrara, J. D., Sondek, J., and Parise, L. V. (2005) *J. Biol. Chem.* **280,** 8407–8415
45. Zhang, M., Tanaka, T., and Ikura, M. (1995) *Nat. Struct. Biol.* **2,** 758–767
46. Kuboniwa, H., Tjandra, N., Grzesiek, S., Ren, H., Klee, C. B., and Bax, A. (1995) *Nat. Struct. Biol.* **2,** 768–776
47. Finn, B. E., Evenas, J., Drakenberg, T., Waltho, J. P., Thulin, E., and Forsen, S. (1995) *Nat. Struct. Biol.* **2,** 777–783
48. Herzberg, O., and James, M. N. (1988) *J. Mol. Biol.* **203,** 761–779
49. Andersson, M., Malmendal, A., Linse, S., Ivarsson, I., Forsen, S., and Svensson, L. A. (1997) *Protein Sci.* **6,** 1139–1147
50. Malmendal, A., Evenas, J., Thulin, E., Gippert, G. P., Drakenberg, T., and Forsen, S. (1998) *J. Biol. Chem.* **273,** 28994–29001
51. Moncrief, N. D., Kretsinger, R. H., and Goodman, M. (1990) *J. Mol. Evol.* **30,** 522–562
52. Iwai, M., Michikawa, T., Bosanac, I., Ikura, M., and Mikoshiba, K. (2007) *J. Biol. Chem.* **282,** 12755–12764
53. Chen, R., and Weng, Z. (2002) *Proteins* **47,** 281–294
54. Bosanac, I., Alattia, J. R., Mal, T. K., Chan, J., Talarico, S., Tong, F. K., Tong, K. I., Yoshikawa, F., Furuichi, T., Iwai, M., Michikawa, T., Mikoshiba, K., and Ikura, M. (2002) *Nature* **420,** 696–700
55. Bosanac, I., Yamazaki, H., Matsu-Ura, T., Michikawa, T., Mikoshiba, K., and Ikura, M. (2005) *Mol. Cell* **17,** 193–203
56. Patterson, R. L., van Rossum, D. B., Barrow, R. K., and Snyder, S. H. (2004) *Proc. Natl. Acad. Sci. U. S. A* **101,** 2328–2332
57. Hoeflich, K. P., and Ikura, M. (2002) *Cell* **108,** 739–742
58. Dick, I. E., Tadross, M. R., Liang, H., Tay, L. H., Yang, W., and Yue, D. T. (2008) *Nature* **451,** 830–834